Submitted to *Earth and Planetary Science Letters*

January 28, 2005

Revised version submitted on June 13, 2005

Radiation-induced decomposition of U(VI) phases to nanocrystals of UO_2

Satoshi Utsunomiya[a], Rodney C. Ewing[a,b,c,*] and Lu-Min Wang[b,c]

[a]*Department of Geological Sciences*

[b]*Department of Nuclear Engineering and Radiological Sciences*

[c]*Department of Materials Science & Engineering*

The University of Michigan

Ann Arbor, MI 48109-1005, USA

*Corresponding author. Tel.: +1 734 7639295; fax: +1 734 647 5706.

E-mail address: rodewing@umich.edu

Abstract

U^{6+}-phases are common alteration products, under oxidizing conditions, of uraninite and the UO_2 in spent nuclear fuel. These U^{6+}-phases are subjected to a radiation field caused by the α-decay of U, or in the case of spent nuclear fuel, incorporated actinides, such as ^{239}Pu and ^{237}Np. In order to evaluate the effects of α-decay events on the stability of the U^{6+}-phases, we report, for the first time, the results of ion beam irradiations (1.0 MeV Kr^{2+}) of U^{6+}-phases. The heavy-particle irradiations are used to simulate the ballistic interactions of the recoil-nucleus of an α-decay event with the surrounding structure. The Kr^{2+}-irradiation decomposed the U^{6+}-phases to UO_2 nanocrystals at doses as low as 0.006 displacements per atom (dpa). U^{6+}-phases accumulate substantial radiation doses (~1.0 displacement per atom) within 100,000 years if the concentration of incorporated ^{239}Pu is as high as 1 wt%. Similar nanocrystals of UO_2 were observed in samples from the natural fission reactors at Oklo, Gabon. Multiple cycles of radiation-induced decomposition to UO_2 followed by alteration to U^{6+}-phases provide a mechanism for the remobilization of incorporated radionuclides.

Keywords

U(VI)-phase, ion irradiation, uraninite, nanocrystals, Oklo,

1. Introduction

Spent nuclear fuel consists primarily of UO_2 (> 95 wt%), and the balance, depending on the burn-up is ~ 1% Pu, 2-3% fission product elements and small amounts of other transuranium elements, such as ^{237}Np (a result of a-decay of ^{241}Am). Under oxidizing conditions, the UO_2 will alter in the presence of water to an assemblage of U^{6+}-phases [1-3]. During the alteration of UO_2, radionuclides are released, but some, particularly actinides, such as long-lived ^{239}Pu (half-live = 24,100 years) and ^{237}Np (half-life = 2.1 million years), may be re-incorporated into the U^{6+}-phases [4]. Thus, these secondary, U^{6+} phases become "sinks" for actinides, delaying their transport to the biosphere and lowering their contribution to the calculated doses in performance assessments of geologic repositories [5,6].

Recently, there has been an increased effort to understand the paragenesis of the U^{6+}-alteration phases of UO_2 [7] and their stabilities [8] in order to better understand their role in controlling the mobility of radionuclides released during the corrosion of UO_2[9]. The major focus of recent experimental studies has been on the incorporation of very long-lived actinides, such as ^{237}Np (half-life = 2.1 million years), into U^{6+}-phases [10-13], because ^{237}Np is a major contributor to calculated dose at long times. However, radiation damage by α-decay of actinides causes atomic displacements that lead to amorphization [14] and radiation-enhanced diffusion of trace elements, similar to the radiation-enhanced loss of fission product elements in UO_2 [15]. Although the α-particles dissipate most of their energy by electronic interactions, causing a minimal amount of radiation-enhanced diffusion due to the limited number of atomic displacements [16], the α-recoil nucleus dissipates most of its energy by ballistic interactions that can cause more than 1,000

atomic displacements for a single α-decay event. While there has been considerable effort devoted to studying radiation effects in spent nuclear fuel [17] and nuclear waste forms [14,18], there has been almost no investigation of the effect of radiation on the corrosion products of UO_2. During the first several hundred years after disposal, the radiation field is dominated by the highly ionizing β- and γ-radiation with doses between 10^8 to 10^6 Gy/y [19]. The effects of ionizing radiation on uranophane, $Ca[(UO_2)(SiO_3OH)]_2(H_2O)_5$, were previously investigated using a 200 keV electron beam over 95 to 573 K [20]. The radiation doses required to cause amorphization varied slightly with the composition of the uranophane (Sr and Eu were substituted for Ca) but were generally in the range 10^{10} Gy. The dose required for amorphization increased by one order of magnitude (10^{11} Gy) above 413 K due to the loss of structural water. These cumulative doses and dose rates in the experiment are much higher (by three orders of magnitude and seven to ten orders of magnitude, respectively) than that experienced by spent nuclear fuel; hence, ionizing radiation is not expected to have a significant effect on the U^{6+}-phases that form on the surfaces of corroded nuclear fuel. However, beyond several hundred years, the principal source of radiation is from α-decay events in the actinide decay chains. For the U^{6+}-phases formed on spent nuclear fuel the accumulated doses are dominated by the α-decay of ^{238}U, ^{235}U, and minor concentrations of ^{239}Pu and ^{237}Np. The recoil nucleus in an α-decay event has an energy of ~0.1 MeV and produces approximately 1,200 Frenkel pair defects along a stopping distance of 30 to 50 nm, creating a displacement cascade about 5 nm in size. The density of energy deposited into the crystal structure by an α-recoil cascade is very high, up to 1 eV/atom, and energy-deposition occurs over a very short time, $<10^{-12}$ s. The cumulative doses for the pure U^{6+}-

phases, e.g., uranophane, at 0.1 and 1 m.y. are calculated, using SRIM2003 [21], to be 0.009 and 0.09 dpa (displacements per atom; see appendix for details of the calculation). However, with the incorporation of 1 wt.% ^{239}Pu, the doses may reach 0.27 and ~1.00 dpa in ten thousand and one hundred thousand years, respectively. The damage production process can cause the formation of point defects, defect clusters, amorphous domains, metastable phases, and elemental segregation into bubbles, surfaces and grain boundaries. These ballistic interactions can be simulated by charged-particle irradiations, typically with 0.5 to 1.5 MeV Xe, Kr, Ar and Pb ions, observed *in situ* by transmission electron microscopy [14,22]. Consistent results have been obtained in comparison to results from actinide-doping experiments [23].

In this study, we have used 1.0 MeV Kr^{2+} irradiations to simulate the ballistic interactions of the α-recoil nucleus with different U^{6+}- phases (Table 1). These U^{6+}-phases are typical of the minerals that occur as the secondary, uranyl-alteration phases that form under oxidizing conditions at uranium ore deposits. Uranophane and boltwoodite have been observed to form in laboratory studies of the alternation of spent nuclear fuel [2,24]. The other phases were selected so as to have a variety of uranyl structure types (Figure 1). These U^{6+}-phases generally form sheets of edge- and corner-sharing U-coordination polyhedra with the larger, inter-layer cations, such as Ca or K, located between the sheets of U-coordination polyhedra [25,26]. Liebigite is not a sheet structure, forming instead isolated clusters (Figure 1d). In Figure 1, we also include the schematic of the three-dimensional structure of UO_2, a fluorite structure-type in which U^{4+} is in cubic coordination, and one-half of the cubic sites are empty.

2. Methods

Target materials of secondary uranyl-minerals for the present irradiation experiments were characterized by powder X-ray diffraction analysis (XRD) to minimize the contamination by other phases and also confirmed by selected area electron diffraction (SAED) in TEM (transmission electron microscopy) (left plates in Fig. 2). All of the x-ray diffraction peaks belonged to the pure uranyl-phase that was identified in each XRD pattern, except that the uranophane contained a small amount of sklodowskite which has a same structure as uranophane, but with the substitution Mg for Ca. Because of the small amount of the carnotite sample, XRD analysis could not be done. The TEM observation revealed no contamination of uraninite in any of the target materials. Liebigite was unstable under minimum electron beam irradiation. Thus, the SAED of liebigite is not shown in Fig. 2. TEM characterization was completed using a JEOL 2010F. The acceleration voltage is 200 kV and the spherical aberration coefficient is 1.0 mm. Scanning TEM imaging and elemental mapping were also completed using the same instrument with 0.5 nm of the spot size. A drift correction mode was used during the acquisition of data. All of the samples were irradiated with *in situ* TEM observation using 1.0 MeV Kr^{2+} in the IVEM (intermediate-voltage electron microscope) at the IVEM-Tandem Facility of Argonne National Laboratory. The ion flux was 6.3×10^{11} ions/cm^2/sec. The specimen temperatures during irradiation were 298 and 673 K, respectively. The structural transition was observed by SAED. The electron beam was off during the ion irradiation, and only used for short intervals during the ion irradiation. In this way, the effect of electron beam was minimized and negligible, because prior electron irradiation experiments on these uranyl minerals only showed amorphization at

electron fluences as high as 2×10^{21} e^-/cm^2. Ion fluence was converted to dpa using SRIM2000 [21]. The displacement energies, E_d, were assumed to be 40 eV for U [14], 23 for P and Si [14], 28 eV for O [14], 10 eV for H [21], 20 eV for C [21] and 25 eV for interlayer cations and V [21].

In addition, a natural uraninite and the surrounding alteration phase were observed using TEM to compare the nanostructure with the results of irradiation experiments. The sample was collected from reactor zone 9 in the 2.0 b.y.-old natural fission reactor at Oklo, Gabon [27]. The reactor zone 9 is located at 140 m of the depth in Oklo open pit. The sample is typically described to contain uraninite, coffinite, and abundant of organic matter [27].

3. Results and discussion

During 1.0 MeV Kr^{2+} irradiation of uranophane, both at room temperature and 673 K, some areas decomposed at an ion fluence of 1.25 x 10^{13} ions/cm^2 (0.014 dpa). Diffraction maxima in SAED pattern became diffuse and disappeared, but a pattern of diffraction rings appeared. Irradiation at elevated temperature (673 K) also showed the transition to ring patterns in the SAED. All of the radiation-induced ring patterns including those revealed at elevated temperature were identified as uraninite (in Fig. 2) without any evidence of other crystalline phases. The diffraction pattern of kasolite revealed some intense diffraction maxima that indicate a preferred orientation for the crystallites or a large crystalline size, >100nm, but the pattern was still identified as uraninite. There was some variation in the nucleation of uraninite nanocrystals as a function of fluence even in the same phase at different positions within sample. Most of the U^{6+}-phase decomposed

to polycrystals of uraninite at ~10^{13}-10^{14} ion/cm^2. The range of the ion fluences was equivalent to 0.006-0.2 dpa. The minimum dose for the formation of nanocrystals of UO_2 in uranophane was 0.006 dpa. Because the radiation-induced structural transformation was most clearly recognized in boltwoodite, the results for boltwoodite are given in detail.

Figure 3a shows the radiation-induced transition as evidenced in the SAED pattern in boltwoodite from 0 to 1.37 dpa on Kr^{2+}-irradiation at 298 K. The boltwoodite retained a euhedral, needle-like crystal form after irradiation; however, the entire crystal was completely converted to an aggregate of uraninite nanocrystals at the dose of 1.37 dpa (Fig. 3b). High-resolution TEM (HRTEM) images revealed that the nanocrystals vary in size: >20 nm (Fig. 3c) and the smallest was <5 nm (Fig. 3d). In addition, amorphous domains were present at the boundaries of uraninite nanocrystals (Fig. 3d). Following the formation of uraninite nanocrystals from uranyl alteration phases, the other cations; Si and K, should be present within amorphous domains. The sequence of events for the formation of the nanocrystals of uraninite may be described as: (i) Decomposition of uranyl-minerals to UO_2 in the displacement cascades created by ion irradiation. (ii) Rapid nucleation of uraninite nanocrystals in the highly disordered "melt-like" displacement cascade. The nano-scale size of the recrystallized uraninite is probably due to rapid "quenching" within the cascades. Indeed, irradiation-induced nanocrystallization is frequently reported to be associated with decomposition and nucleation processes [28].

The bright-field (BF)-scanning TEM image of boltwoodite after 1.37 dpa of accumulated dose at 298 K is shown in Fig. 4a with elemental maps for Si and U. Particles in dark contrast are uraninite nanocrystals, and the matrix (brighter contrast) is amorphous. Because the K_α line of potassium in the EDS overlaps the U-M line, the K-

map is not shown in Fig. 4a. However, the elemental map shows that Si is distributed in the amorphous region present at the grain boundary of the uraninite. Uraninite nanocrystals and an amorphous matrix in the grain boundaries were observed in the other uranyl-minerals after ion irradiation, which is supported by the observation that each diffraction pattern revealed only the ring pattern of uraninite (Fig.2). Thus, the other uranyl-minerals also had the amorphous domains at the grain boundaries of uraninite nanocrystals that contained the constituent cations, e.g., K and Ca, that were present prior to the radiation-induced decomposition of the uranyl-minerals.

Clearly, the nanocrystals of uraninite were produced by ion irradiation and decomposition of these uranyl-minerals. However, there are differences in the conditions between the ion irradiation experiments and α-decay events. The dose rate during the ion irradiation experiments is ~10^{11} times higher than that from α-decay events experienced by naturally occurring U^{6+}-phases. The higher dose rate leads to greater cascade overlap because there is minimum opportunity for relaxation and recovery of defects formed by the cascade. The higher dose rate usually results in an increase in the critical amorphization temperature for materials, T_c, the temperature above which the amorphization does not occur due to thermal annealing [29]. Changes in the energy and species of ion are also considered to result only in shifts of the amorphization dose and T_c [14,28]. Also, the incident ion species used in the present experiments were Kr^{2+} at energy of 1.0 MeV; whereas, in an α-decay event, the recoil nuclei are heavier and have a lower energy. As an example, the recoil nucleus of ^{239}Pu is ^{235}U with the energy of 86 keV [14]. However, these differences are accounted for by the conversion of the ion fluences to displacements per atom using SRIM [21], allowing the comparison of the two

different types of irradiations. Thus, we expect that the ion-beam irradiation results are a reasonable simulation of the ballistic interactions of α-recoil nucleus that have led to the formation of nanocrystals of UO_2.

Uraninites from natural uranium deposits and U^{6+}-alteration products formed under oxidizing conditions were also examined to see if there was evidence for the decomposition and formation of nanocrystals of UO_2, similar to those observed in the ion irradiation experiments. Samples from the 2.0 b.y.-old natural fission reactor at Oklo, Gabon [26] was examined. Using TEM, some uraninites were found as large single crystals at the micron scale, but others were present as aggregates of nanocrystals at both localities. The presence of Si and Mg was also revealed by EDS. The HRTEM image, with corresponding elemental maps of the uraninite from Oklo-Okélobondo, revealed aggregates of nanocrystalline uraninite with the amorphous matrix containing Si at the grain boundaries, a texture similar to that observed in the ion irradiation-induced nanocrystals of uraninite (Fig. 4b). Although it is possible that the uraninite precipitated as a secondary phase under reducing conditions, coffinite, $USiO_4\,nH_2O$, is stable in solutions containing Si; thus, the formation of coffinite is the expected phase in these samples [30]. However, Si is present in the amorphous matrix, with no evidence of the formation of coffinite, and the uraninite nanocrystals are randomly oriented, forming high-angle grain boundaries. In addition, although an aluminosilicate was observed adjacent to the aggregates of uraninite, the uraninite region was Al-free, suggesting that this Si was not associated with the altering solution that caused the formation of the aluminosilicate. Although it is still possible that these uraninite nanocrystals formed by another unkown process, their presence in the Oklo sample is at least consistent with the

radiation-induced decomposition of uranyl-minerals to UO_2 as observed in the ion beam irradiation experiments.

Based on the results of the ion irradiations of U^{6+}-phases, the recoil nucleus of an α-decay event of actinides in secondary uranyl minerals causes the decomposition and nano-scale formation of UO_2. The nanocrystals of UO_2 form at doses as low as 0.006 dpa, which is slightly less than the accumulated dose in pure U^{6+} phases due to self α-decay after 100,000 years, 0.009 dpa. However, the addition of 1 wt.% ^{239}Pu leads to an increase in dose to 0.27 dpa in 10,000 years, well in excess of the dose required for radiation-induced decomposition of the U^{6+}-phases. Thus, one expects, in altered uraninite older than 10,000 years, multiple cycles of radiation-induced decomposition of U^{6+}-phases to nanocrystals of UO_2, followed by re-alteration back to U^{6+}-phases under oxidizing conditions. During these repeated cycles of radiation-damage (i.e., cascade quenching and decomposition to UO_2) and alteration back to U^{6+}-phases, trace elements may be lost by this nano-scale, zone-refining process. Due to the extremely small size and high surface area of the UO_2 nanoparticles, oxidation and alteration back to U^{6+}-phases will generally be rapid. This may explain the rather high purity, relative to trace elements, of the uranyl alteration phases observed in nature. This is also a process by which radionuclides incorporated in U^{6+}-phases may be released and available for transport in the geosphere.

Appendix A. Calculation of cumulative doses in U^{6+}-phase

The number of displacements for each alpha-decay event was calculated using SRIM2003 [21]. The ideal formula is $Ca(UO_2)_2(SiO_3OH)_2 \cdot 5(H_2O)$. The density of uranophane is 3.9 g/cm^3.

		Emitted α-particle			Recoiled daughter nucleus			
^{238}U series		Alpha-energy (MeV)	Range (μm)	Vacancies	Nucleus energy (keV)	Range (Å)	Vacancies	Sum
1	$^{238}U \rightarrow ^{234}Th$	4.198	15.2	156	71.8	296	730	
2	$^{234}U \rightarrow ^{230}Th$	4.775	18.2	158	83	321	835	
3	$^{230}Th \rightarrow ^{226}Ra$	4.688	17.7	161	97.7	357	967	
4	$^{226}Ra \rightarrow ^{222}Rn$	4.784	18.2	160	86.2	330	860	
5	$^{222}Rn \rightarrow ^{218}Po$	5.489	22.2	163	100.7	367	989	
6	$^{218}Po \rightarrow ^{214}Pb$	6.002	25.4	166	112.2	397	1100	
7	$^{214}Po \rightarrow ^{210}Pb$	7.687	36.8	172	146.5	472	1406	
8	$^{210}Po \rightarrow ^{206}Pb$	5.304	21.2	163	103	374	1021	
	Average			162			989	1151
^{235}U series								
1	$^{235}U \rightarrow ^{231}Th$	4.596	17.2	158	73.4	295	742	
2	$^{231}Pa \rightarrow ^{227}Ac$	5.059	19.8	160	89.2	337	890	
3	$^{227}Th \rightarrow ^{223}Ra$	6.038	25.6	167	108.4	381	1062	
4	$^{223}Ra \rightarrow ^{219}Rn$	5.871	24.5	166	107.3	383	1055	
5	$^{219}Rn \rightarrow ^{215}Po$	6.819	30.7	170	126.9	427	1225	
6	$^{215}Po \rightarrow ^{211}Pb$	7.386	34.7	173	140.1	457	1349	
7	$^{211}Bi \rightarrow ^{207}Tl$	6.623	29.4	170	128	431	1237	
	Average			166			1080	1246
								1199
239Pu decay								
	$^{239}Pu \rightarrow ^{235}U$	5.25	20.9	162	86	322	854	1016
	Decay process after ^{235}U formation is same as listed above.							

The damage can be calculated using the mean value for vacancy formation. The simplified equation is;

$$dpa = 1200 \times D_\alpha \times MW / (N_A \times n_{atom})$$

where MW is the molecular weight. N_A is the Avogadro's number, and n_{atom} is the number of atom in molecular formula.

Uranium concentration in uranophane is 55.59 wt%.

$$D_\alpha = \frac{\frac{^{238}U}{^{238}U+^{235}U} \times n_{238U} \times U(ppm)}{238 \times 10^6} \times N_A \times (1 - \exp(-\lambda_{238U} t)) \times \frac{1}{10^3}$$

$$+ \frac{\frac{^{235}U}{^{238}U+^{235}U} \times n_{237U} \times U(ppm)}{238 \times 10^6} \times N_A \times (1 - \exp(-\lambda_{235U} t)) \times \frac{1}{10^3} \text{ (alpha-decay events/mg)}$$

where n_i is the number of alpha decay events per one decay chain of the isotope, i.

Symbols, λ_{238U} and λ_{235U} are the decay constant for ^{238}U and ^{235}U, respectively

T (year)	D_α (α-decay events/mg) in uranophane	dpa
10,000	1.80E+13	0.00090
100,000	1.80E+14	0.0090
1,000,000	1.80E+15	0.090

When 1 wt% of ^{239}Pu (Pu/U=0.018) is incorporated in uranophane, a contribution to the dose by Pu must be added to the total cumulative dose.

$$D_\alpha = \frac{Pu(ppm)}{239 \times 10^6} \times N_A \times (1 - \exp(-\lambda_{239Pu} t)) \times \frac{1}{10^3}$$

$$+ \frac{7 \times Pu(ppm) \times (1 - \exp(-\lambda_{239Pu} t))}{235 \times 10^6} \times N_A \times (1 - \exp(-\lambda_{235U} t)) \times \frac{1}{10^3}$$

The calculated doses are given below. For the case of 1000 ppm of Pu, the dpa's are simply 10 times less than dpa's of 1 wt%.

T (year)	D_α (α-decay events/mg) in uranophane	dpa
10,000	6.30E+15	0.27
100,000	2.38E+16	1.01
1,000,000	2.54E+16	1.08

For the ^{237}Np decay series, we have assumed that the number of vacancies created per ion is ~1200 (comparable to those for the a-decay of other actinides). When 0.02 wt% of Np (Np/U=0.00036) is incorporated into uranophane, the dose contribution due to α-decay in the ^{237}Np-series is calculated to be:

T (year)	Dose (alpha-decay events / mg)	dpa
10,000	1.00E+13	0.00050
100,000	9.88E+13	0.0050
1,000,000	8.73E+14	0.044

Acknowledgements

The authors thank the staff of the IVEM-Tandem Facility at Argonne National Laboratory for assistance during the ion irradiation experiments. S.U. thanks J. F. Mansfield and C. J. Wouchope of the Electron Microbeam Analysis Laboratory at University of Michigan. This work was initiated with support by US DOE, Office of Basic Energy Sciences under grant DE-FGO7-97ER14816, with continuing support from Office of Science and Technology and International (OSTI) of the Office of Civilian Radioactive Waste Management (DE-FE28-04RW12254). The views, opinions, findings, and conclusions or recommendations of the authors expressed herein do not necessarily state or reflect those of the DOE/OCRWM/OST&I.

References

[1]. R. J. Finch, R. C. Ewing, *J. Nucl. Mater.* **190,** 133 (1992).

[2]. D. J. Wronkiewicz, J. K. Bates, T. J. Gerding, E. Veleckis, B. S. Tani, *J. Nucl. Mater.* **190,** 107 (1992).

[3]. R. J. Finch, T. Murakami, in *Uranium –Mineralogy, Geochemistry and the Environment*, P. C. Burns, R. J. Finch, Eds. *Rev. Miner.* **38**, 91 (1999).

[4]. P. C. Burns, R. C. Ewing, M. L. Miller, *J. Nucl. Mater.* **245**, 1 (1997).

[5]. E. Curti, *Coprecipitation of radionuclides: basic concepts, literature review and first applications*, Paul Scherrer Institut, Bericht Nr. 97-10. p107 (1997).

[6]. Y. Chen, *Computers & Geoscience,* **29,** 385 (2003).

[7]. D. Wronkiewiecz, E. Buck, in *Uranium –Mineralogy, Geochemistry and the Environment*, P. C. Burns, R. J. Finch, Eds. *Rev. Miner.* **38**, 475 (1999).

[8]. F. Chen, R. C. Ewing, S. B. Clark, *Am. Mineral.* **84,** 650 (1999).

[9]. W. M. Murphy, R. B. Codell, *Mater. Res. Soc. Proc.* **556,** 551 (1999).

[10]. E. Buck, R. J. Finch, P. A. Finn, J. K. Bates, *Mater. Res. Soc. Proc.* **506,** 87 (1998).

[11]. P. C. Burns, K. M. Deely, S. Skanthakumar, *Radiochim. Acta* **92,** 151 (2004).

[12]. M. Douglas, S. B. Clark, J. I. Friese, B. W. Arey, E. C. Buck, B. D. Hanson, S. Utsunomiya, R. C. Ewing, *Radiochim. Acta* **93,** 265 (2005).

[13]. M. Douglas, S. B. Clark, J. I. Friese, B. W. Arey, E. C. Buck, B. D. Hanson, *Environ. Sci. Technol.* in review.

[14]. W. J. Weber, *et al., J. Mater. Res.* **13**, 1434 (1998).

[15]. H. Matzke, *Rad. Eff. Def. Solid.* **64,** 3 (1982).

[16]. L. Desgranges, M. Ripert, J. P. Piron, H. Kodja, J. P. Gallier, *J. Nucl. Mater.* **321,** 324 (2003).

[17]. H. Matzke, L. M. Wang, L.M. *J. Nucl. Mater.* **231**, 155 (1996).

[18]. R. C. Ewing, W. J. Weber, J. Lian, *J. Appl. Phys.* **95,** 5949 (2004).

[19]. D. W. Shoesmith, *J. Nucl. Mater.* **282,** 1 (2000).

[20]. S. Utsunomiya, L. M. Wang, M. Douglas, S. B. Clark, R. C. Ewing, *Am. Min.* **88,** 159 (2003).

[21]. J. F. Ziegler, J. P. Biersack, U. Littmark, *The stopping and range of ions in solids* (Pergamon, New York, 1985).

[22]. L. M. Wang, R. C. Ewing, *Mater. Res. Soc. Bull.* **17**, 38 (1992).

[23]. W. J. Weber, R. C. Ewing, *Science* **289**, 2051 (2000).

[24]. D. J. Wronkiewicz, J. K. Bates, S. F. Wolf, E. C. Buck, *J. Nucl. Mater.* **238,** 78 (1996).

[25]. P. C. Burns, in *Uranium –Mineralogy, Geochemistry and the Environment*, P. C. Burns, R. J. Finch, Eds. *Rev. Miner.* **38**, 23 (1999).

[26]. P. C. Burns, M. L. Miller, R. C. Ewing, *Can. Mineral.* 34, 845 (1996).

[27]. K. A. Jensen, R. C. Ewing, *GSA Bull.* **113**, 32 (2001).

[28]. L. M. Wang, *et al.*, *Mater. Sci. Eng. A* **286**, 72 (2000).

[29]. S. X. Wang, L. M. Wang, R. C. Ewing, *Phys. Rev. B* **63**, 024105, (2000).

[30]. J. Janeczek, R. C. Ewing, *J. Nucl. Mater.* **190**, 157-173 (1992).

Figure captions

Fig. 1. Schematic diagrams of the anion topologies of the uranyl-minerals of this study. (a) Uraninite. (b) Uranyl silicates including boltwoodite, uranophane and kasolite viewed along the a-axis. (c) Uranyl vanadate, carnotite along a-axis. (d) Uranyl carbonate, liebigite along c-axis. (e) Uranyl phosphate, saléeite along b-axis.

Fig. 2. The SAED patterns before and after 1.0 MeV Kr^{2+} irradiation at the room temperature. uranophane 0 -> 0.77 dpa. kasolite, 0 -> 2.2 dpa. carnotite, 0 -> 0.11 dpa. saléeite, 0 -> 1.0 dpa. liebigite after 0.85 dpa. The white arrows indicate the position of the ring diffraction pattern for the polycrystalline uraninite.

Fig. 3. Boltwoodite under Kr^{2+} irradiation (1.4 dpa) at room temperature. (a) the transition as evidenced in the SAED. (b) TEM image shows a needle-like shape of the original boltwoodite crystal. HRTEM reveals a large aggregate of uraninite nanocrystals. The size ranges from >20 nm (c) to <5 nm (d). The uraninite nanocrystals are in a random orientation and the surrounding matrix is amorphous (d).

Fig. 4. (a) Bright-field STEM image of boltwoodite after 1.0 MeV Kr^{2+} irradiation of 1.4 dpa at room temperature with elemental maps of U and Si. (b) HRTEM image of natural uraninite from Oklo, Gabon, with elemental maps of U and Si, showing aggregates of uraninite nanocrystals randomly oriented with high-angle grain boundaries. Note the amorphous matrix at the grain boundaries, which is similar to the texture created by the ion-irradiation experiments.

Table 1. U^{6+}-phases irradiated by 1.0 MeV Kr^{2+}

β-uranophane	$Ca[(UO_2)(SiO_3OH)]_2(H_2O)_5$	$P2_1/a$; Z=2
boltwoodite	$K[(UO_2)(SiO_3OH)](H_2O)_{1.5}$	$P2_1/m$; Z=2
kasolite	$Pb[(UO_2)(SiO_4)](H_2O)$	$P2_1/c$; Z=4
saléeite	$Mg[(UO_2)(PO_4)]_2(H_2O)_{10}$	$P2_1/c$; Z=2
carnotite	$K_2(UO_2)_2(V_2O_8)(H_2O)_3$	$P2_1/a$; Z=2
liebigite	$Ca_2[(UO_2)(CO_3)_3](H_2O)_{11}$	$Bba2$; Z=8

Figure 1

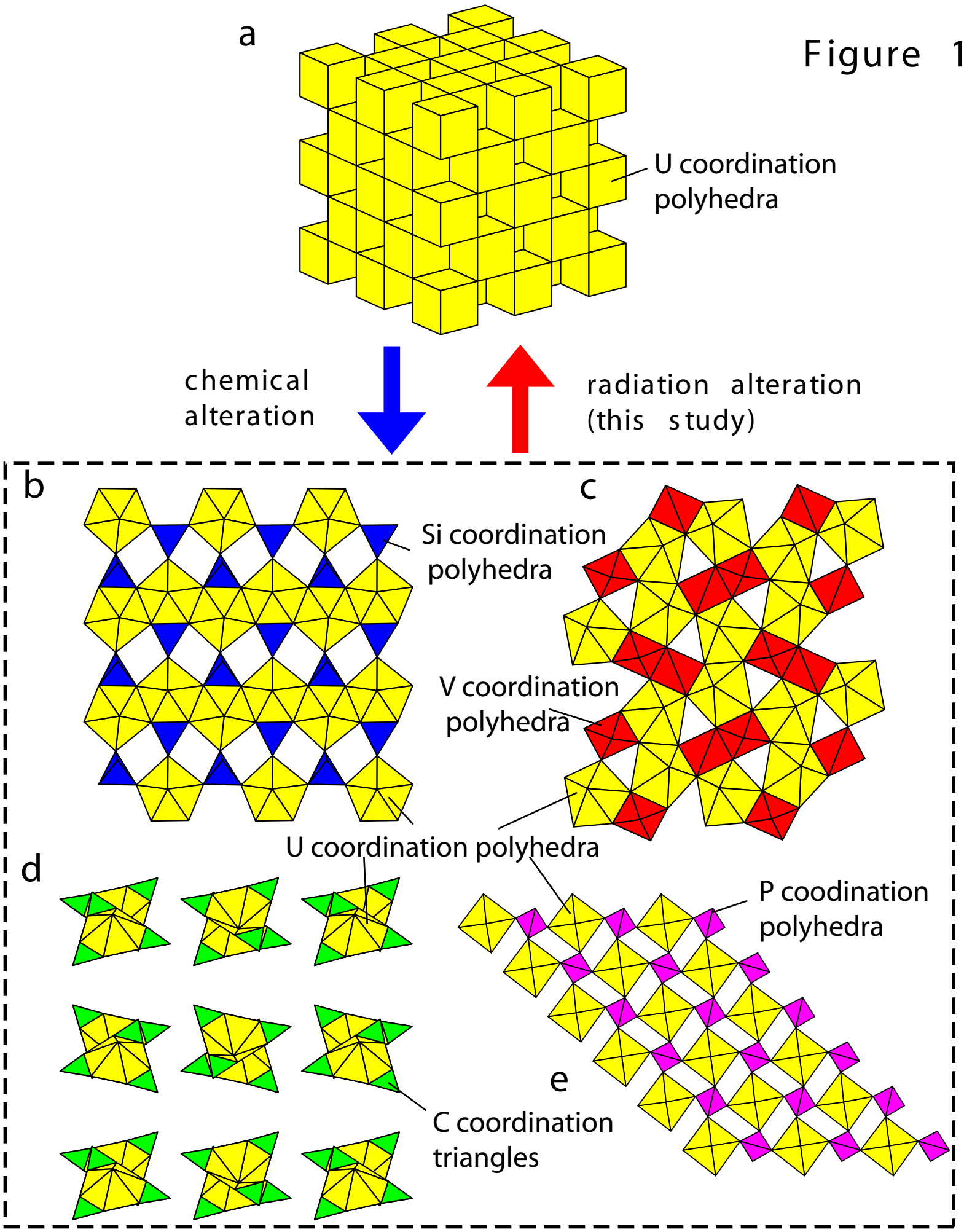
a
U coordination polyhedra
chemical alteration
radiation alteration (this study)
b
Si coordination polyhedra
c
V coordination polyhedra
U coordination polyhedra
d
C coordination triangles
e
P coodination polyhedra

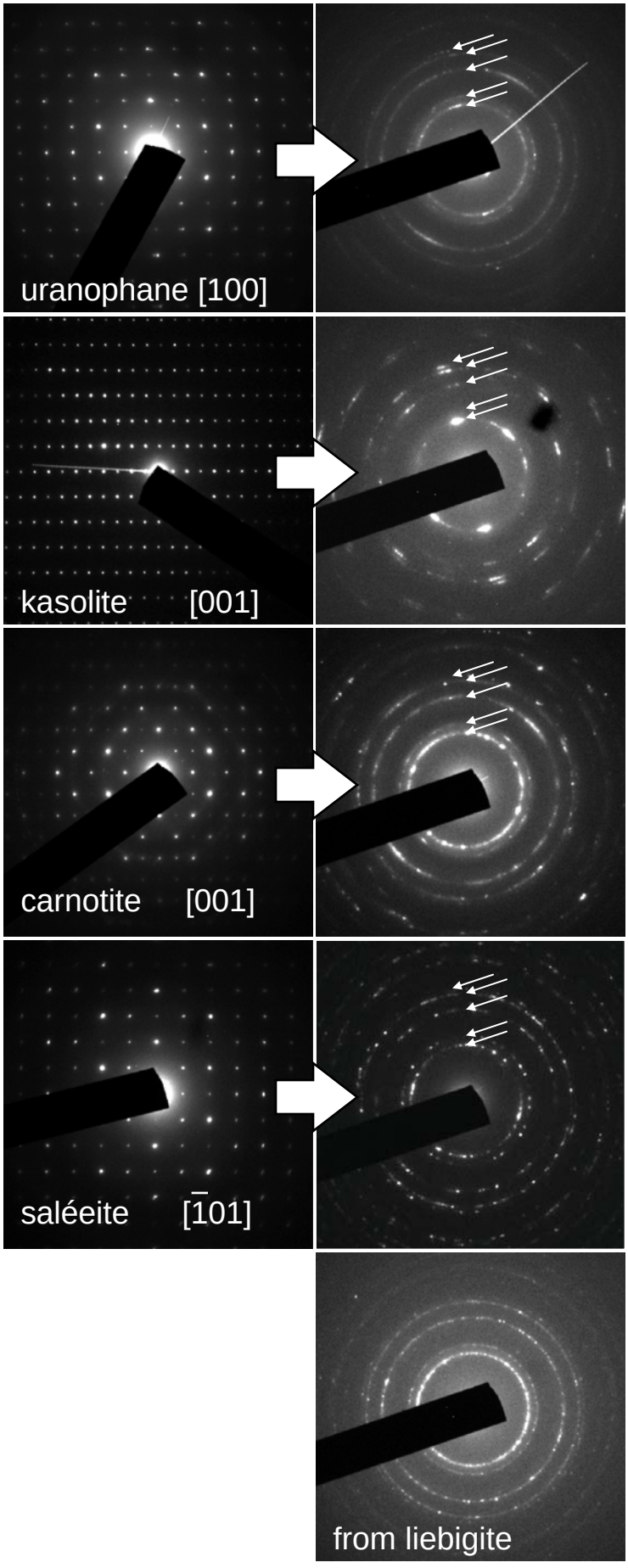
uranophane [100]
kasolite [001]
carnotite [001]
saléeite [$\bar{1}01$]
from liebigite

Figure 2

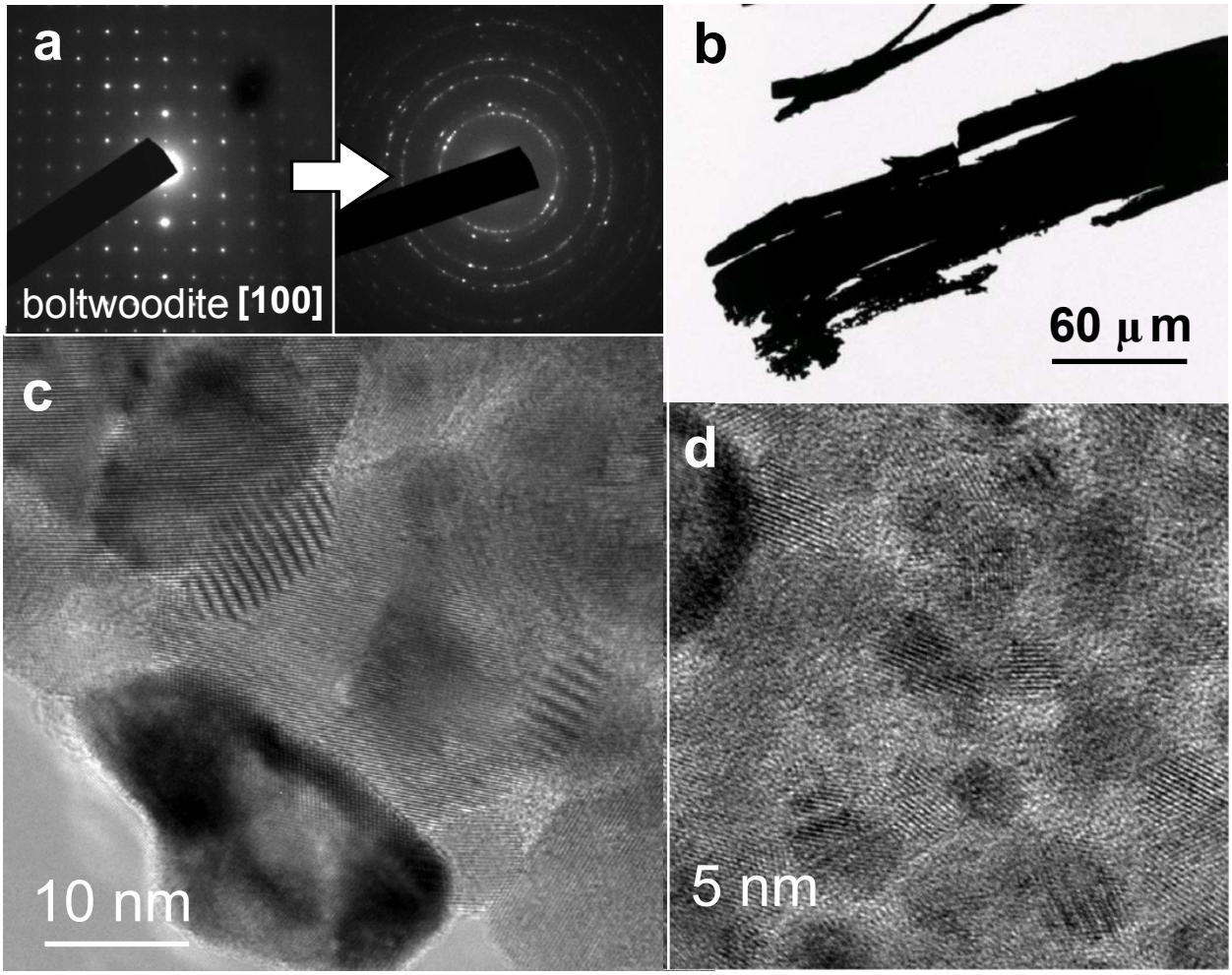

Figure 3

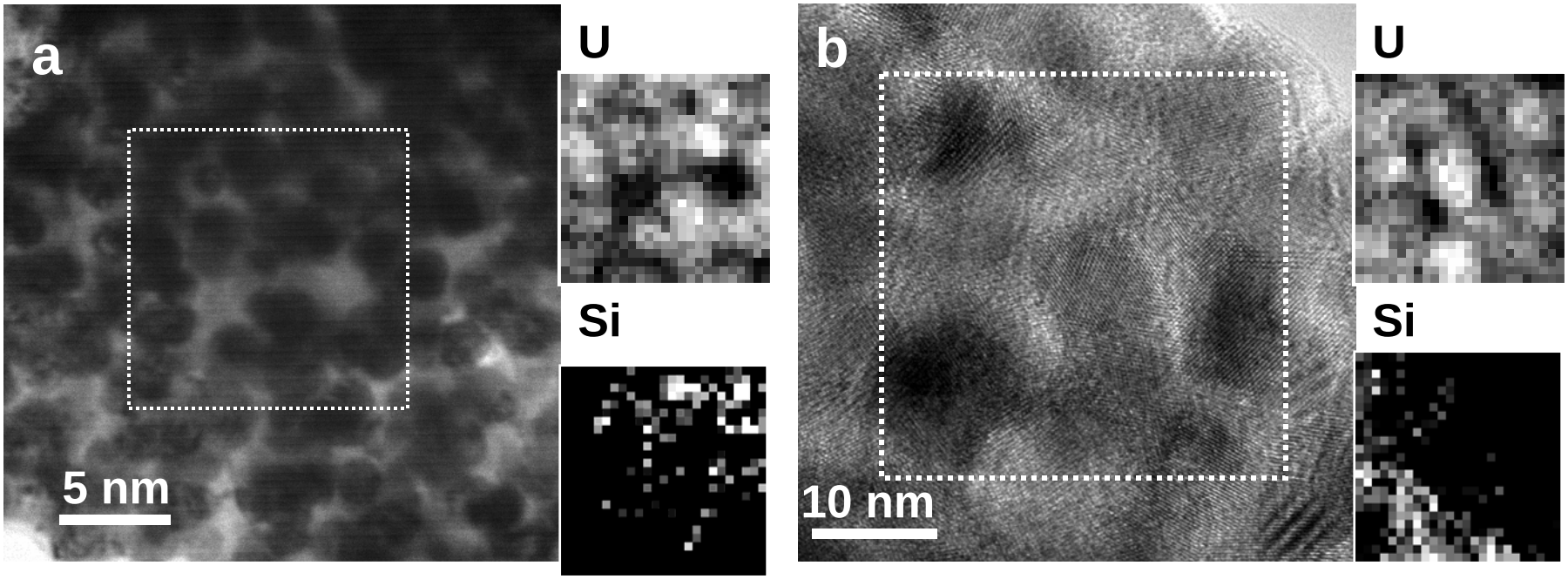

Figure 4